

Received 10 November 2024, accepted 10 December 2024, date of publication 24 December 2024, date of current version 31 December 2024.

Digital Object Identifier 10.1109/ACCESS.2024.3522059



Wireless Pressure Sensing Smart Stent for Enhanced Post-Endovascular Aneurysm Repair (EVAR) Surveillance

JUN YING TAN[®]1, (Member, IEEE), CHEOLBOK KIM², TRISHA DAS MOU[®]3, ALBERT KIM[®]3, AND JUNGKWUN 'JK' KIM¹⁰, (Member, IEEE)
Department of Electrical Engineering, University of North Texas, Denton, TX 76207 USA

Corresponding author: Jungkwun 'Jk' Kim (Jungkwun.Kim@unt.edu)

This work was supported in part by the National Science Foundation (NSF) under Grant CNS 2039014, Grant ECCS 2326938, Grant ECCS 2325032, Grant ECCS 2306330, and Grant ECCS 2245092; and in part by Korea Evaluation Institute of Industrial Technology (KEIT) under Grant 20018023.

ABSTRACT Continuous post-endovascular aneurysm repair (EVAR) surveillance is critical for patients who have undergone a stenting procedure. Despite its life-saving importance, studies have reported that patients gradually discontinue post-EVAR surveillance due to the significant burden associated with CT scans, X-rays, etc. Considering the importance and necessity of post-EVAR surveillance, we introduce a self-resonating flexible tube implanted in a standard clinically approved stent that enables wireless sensing of blood pressure inside an aneurysm through inductive coupling. To enable blood pressure monitoring outside the body, we designed and fabricated a spiral-type antenna, specifically crafted to capture the inherent resonance frequency of the self-resonating stent tube. To showcase the wireless pressure monitoring capability, a 3D-printed elastic model of an abdominal aortic aneurysm (AAA) was prepared. Our quantitative study validated the pressure-sensing capability with adequate sensitivity (up to 687.5 Hz/mmHg) when tissue was located between the stent and the external antenna. The wireless sensing also presents a consistent linear shift in resonance frequency across all tested measuring distances as the applied pressure ranges from 60 to 140 mmHg. The proposed self-resonating stent offers promising insights for improving post-EVAR surveillance.

INDEX TERMS Smart stent, post-EVAR surveillance, wireless pressure monitoring, piezoelectric, selfresonating.

I. INTRODUCTION

The abdominal aortic aneurysm (AAA) is defined as an abnormal dilation of the abdominal aorta, with diameters typically ranging from 3 cm to 7.8 cm, a substantial deviation from the normal dimensions of the abdominal aorta, which generally measures around 1.8 to 2.8 centimeters as it extends from the diaphragm to the level of the pelvis. [1], [2], [3]. The AAA is frequently found in older age, male sex, tobacco use, and a family history of vascular aneurysms, including

The associate editor coordinating the review of this manuscript and approving it for publication was Michail Kiziroglou.

conditions like hypertension, hypercholesterolemia, and coronary artery disease [1], [4]. If AAA is left untreated, the aneurysm sac continues to grow, progressively weakening the arterial wall and eventually leading to rupture. This deterioration can lead to severe internal bleeding, accompanied by a heightened risk of morbidity and mortality. As of today, the treatment of AAA and prevention of AAA-related rupture predominantly involve the implementation of endovascular aneurysm repair (EVAR) via surgical intervention [5], [6]. This procedure entails the insertion of a fabric-covered stent graft into the dilated aorta segment to redirect the blood flow away from the weakened arterial wall.

²Corning Incorporated, Corning, Painted Post, NY 14870, USA

³Department of Medical Engineering, University of South Florida, Tampa, FL 33620, USA

However, the risk of rupture and subsequent late complications stemming from the malfunction of EVAR, including stent migration, structural disintegration, endoleaks, and aneurysm growth [7]. Thus, lifelong post-EVAR surveillance is advised to regularly track the aneurysm's growth and assess the necessity for intervention [7], [8]. In this regard, computed tomography (CT) scanning and magnetic resonance angiography (MRA) have been the gold standard for post-EVAR surveillance [9]. However, patients have limited tolerance for this extended monitoring. In accordance with a clinical research study, 22% of the patients discontinued post-EVAR surveillance within the first year following EVAR, 38% in the third year, and 50% in the fifth year [10]. Such discontinuation of post-EVAR surveillance is due to the significant burden on the patients, including but not limited to the high cost and protracted procedure time associated with each clinical visit. Other noteworthy factors include concerns regarding the risks of contrast-induced nephropathy and carcinogenesis from cumulative radiation exposure [11].

To address the above-mentioned shortcomings, the Smart Stent concept gained considerable interest [12], [13], [14]. These stents, equipped with sensing and monitoring capabilities, have the potential to reduce the cost associated with post-EVAR surveillance, minimize hospital visits, and enhance the overall quality of patient care [15]. For example, Park et al. demonstrated a smart stent device that can wirelessly monitor blood vessel pressure [16]. This device employs a biodegradable polymer-based stent with a pressure sensor, fabricated via a microelectromechanical (MEMS)-based process. They reported that the proposed device demonstrated a high linearity of frequency from 137 to 150 MHz in the pressure range of 0 to 120 mmHg, with a sensitivity of 50 kHz/mmHg. Another example of a potential smart stent device was presented by Liu et al. [17]. Their work demonstrated a stent antenna prototype for intravascular monitoring and implantable wireless applications. They reported that the stent antenna exhibited an omnidirectional radiation pattern and a good radiation efficiency of 74.5%, both of which are promising and useful characteristics for forthcoming implantable wireless communication applications. Another interesting study by Occhiuzzi et al. explored the feasibility of implanted passive radio frequency identification (RFID) to monitor biological processes and detect specific electromagnetic changes caused by evolving biological phenomena (i.e., detecting early stages of restenosis in stents). The design can also be extended to other implanted metal devices like prostheses, sutures, grafts, or orthopedic fixings, offering potential benefits in long-term patient monitoring and personal healthcare systems [18].

However, despite the successful demonstration of wireless pressure sensing in the aforementioned studies, it is important to note that their systems were designed with the ambitious goal of entirely replacing a clinically approved stent graft, currently regarded as the gold standard. This ambitious endeavor underscores the practical challenges and complexities involved in implementing their previous work or devices in real-world clinical settings. Recognizing the challenges associated with the complete replacement of clinically approved stent-grafts, we aimed to devise a more practical and adaptable solution. Our innovation revolves around a modular pressure sensor concept, one that seamlessly integrates into the existing infrastructure of conventional stent grafts. This transformative approach empowers these medical devices with smart capabilities without necessitating a wholesale change in established clinical procedures. Our modular self-resonating pressure sensor, named the smart stent, was constructed using a piezoelectric thin film featuring a strategically designed array of perforations, offers several advantages, as conceptually illustrated in Fig. 1. Given the varying effects of the perforation shape of the piezoelectric thin film, we previously investigated the perforation design for voltage generation and sensitivity to pressure change at a low-frequency range (1 to 1.67 Hz or 60 to 100 beats per minute) [19], [20]. While our primary focus remains on enabling wireless interrogation of pressure within aneurysms, we have also delved into the resonance frequency shift of the perforated piezoelectric membrane under varying pressure conditions. In theory, the smart stent behaves capacitive at DC due to its dielectric properties and configuration [21]. However, as frequency increases, parasitic inductance increases due to various reasons, which in this particular case of smart stent, mainly the skin effect and proximity effect [22]. As the parasitic inductance increases to a point where it balances out the intrinsic capacitance of the smart stent, the smart stent becomes self-resonating, which frequency is known as the resonance frequency. When the smart stent experiences a change in internal pressure, the piezoelectric membrane undergoes a radial expansion. This induced structural deformation by pressure change could cause alternation in several aspects of the piezoelectric membrane such as increased electric charge due to the piezoelectric effect, changes in dielectric constant due to the shifting of dipole alignment, expansion in the physical dimension of the membrane's diameter [23]. The combinations of a series of intricate electrical and mechanical alterations would cause a shifting of the resonance frequency. This shift, detectable through inductive coupling using an external antenna as depicted in Fig. 1, enables our ability to monitor and assess aneurysm status wirelessly. In this article, we present the results of our innovative approach and the quantitative study we conducted to validate the pressure-sensing capabilities of our modular sensor. Our findings demonstrate adequate sensitivity even with the presence of lossy tissue between the stent and the external antenna, providing a promising foundation for improved post-EVAR surveillance.

II. METHODOLOGY

To replicate real-world conditions, our proposed smart stent underwent testing within a closed-loop circulation system designed to mimic the anatomical features of the abdominal aorta, utilizing a 3D-printed model that closely emulates



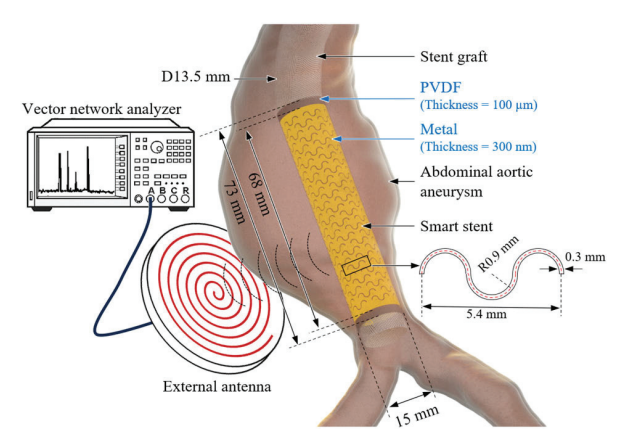


FIGURE 1. Conceptual drawing of the Smart Stent integrated into a stent graft, then implanted into an abdominal aortic aneurysm, in which the Smart Stent serves as a pressure sensor for early detection of potential fatal rupture.

human physiology. The main components of the testing system, as depicted in Fig. 1, consist of a 3D printed AAA model, a custom-made stent graft, and our proposed smart stent. The 3D model of the AAA [24] was 3D printed with modifications using an elastic resin to replicate the elastic characteristics of a human AAA. The stent graft is designed and fabricated based on a commercially available fabriccovered stent graft (Fluency Plus Endovascular Stent Graft) with a diameter of 13.5 mm and a length of 120 mm, which can be securely fitted into the AAA model. The smart stent is designed to have a diameter of 15 mm and a length of 73 mm, which can be integrated into the stent graft. The smart stent is wirelessly coupled with an external antenna and examined across various pressures ranging from 60 to 140 mmHg. Pork bellies with various thicknesses (3 to 7 cm) were placed between the external antenna and the smart stent to replicate the lossy tissues of the human body, and artificial blood from VATA Inc., which has similar viscosity to real blood, was used throughout the examination.

Fig. 2 elucidates the intricate fabrication procedures involved in crafting the self-resonating stent, comprising two fundamental components: the Polyvinylidene fluoride (PVDF) film and the smart stent. The initial step entailed the preparation of a 100- μ m PVDF film, conducted through a casting method as meticulously outlined in [25]. The procedure commenced with the formulation of a 15 wt. % PVDF solution, achieved by combining PVDF powder (Alfa Aesar Chemicals, Inc.) and N, N-Dimethylformamide (DMF) 99% solution (Alfa Aesar Chemicals, Inc.), followed by thorough mixing with a magnetic stirrer at 30 °C for 15 minutes. Subsequently, the solution was subjected to 10 minutes of degassing within a vacuum chamber to eliminate any residual bubbles. As a substrate for film casting, a glass slide measuring 50 mm × 75 mm was employed. It is noteworthy to adjust the substrate's width based on the desired smart stent diameter. Specifically, a 25 mm-wide substrate yields a 7 mm diameter smart stent, a 50 mmwide substrate results in a 15 mm diameter smart stent, and

a 76 mm-wide substrate leads to a 23 mm diameter when rolled into a cylindrical form to fashion a smart stent. The glass substrate underwent treatment with organic solvents (acetone, methanol, and isopropanol) and subsequent oxygen plasma treatment to eliminate organic contaminants, residues, and particles from the surface. Following these preparatory steps, the substrate was coated with 3 g of the prepared PVDF solution and spread evenly. The sample was then annealed at 30 °C for a minimum of 24 hrs within a 30% humidity vacuum chamber. Subsequently, due to its hydrophobic nature, a thin PVDF film was delaminated from the substrate when soaked in deionized (DI) water. The PVDF film was subsequently poled for 1 hr at 5 kV and 80 °C, positioned between two electrodes insulated with Kapton tape. Subsequently, a 100 μ m PVDF film, as depicted in Fig. 2(a), was readied for the ensuing stages.

To fabricate the self-resonating stent, the PVDF film underwent metallization with titanium and copper on both sides, as demonstrated in Fig. 2(b). Initially, a 100 nm thin layer of titanium was deposited onto the film to serve as an adhesion layer, followed by the deposition of a 300 nm thin layer of copper to ensure electrical conductivity. Copper was used in this scenario for experimental purposes; it can be replaced with gold or platinum for biocompatibility. However, further experimentation validation and characterization will be required. The metalized film was then subjected to perforation via a CO₂ laser from Vevor Inc., as depicted in Fig. 2(c). The CO₂ laser was programmatically configured to iteratively create the desired perforation pattern, employing the lowest cutting power (15 W) and the moderate cutting speed (100 mm/s) to achieve optimal cutting precision while safeguarding the integrity of the deposited metal layers. Upon completion of the perforation process, the PVDF film was rolled into a cylindrical shape, in which the margins were adhesively joined using DMF, with the overlapping film area minimized to approximately 3 mm during the rolling process. A gentle compression at the overlapping region was performed using a glass rod to promote adhesion while reducing the PVDF thickness to approximately 100 μ m to ensure uniform expansion over the entire sample. The resultant smart stent exhibited a diameter of approximately 15 mm, slightly larger than the stent graft with a diameter of 13.5 mm. Conclusively, the smart stent underwent passivation with a biocompatible polymer, polydimethylsiloxane (PDMS) via immersion in a PDMS solution, allowing excess PDMS to freely drip off at room temperature for 30 min, followed by rolling the sample on a flat surface to minimize the disparity in the PDMS coating due to the vertical mounting of the sample during the dripping process. Subsequently, the sample was cured in a 60 °C convection oven for 24 hrs, as represented in Fig. 2(e). Despite the efforts, the described process does not guarantee absolute uniformity in the PDMS coating, with a final measured thickness of 92 μ m and 108 μ m at the top and lower ends, respectively. The fully realized smart stent is presented in Fig. 2(f).

VOLUME 12, 2024 198125

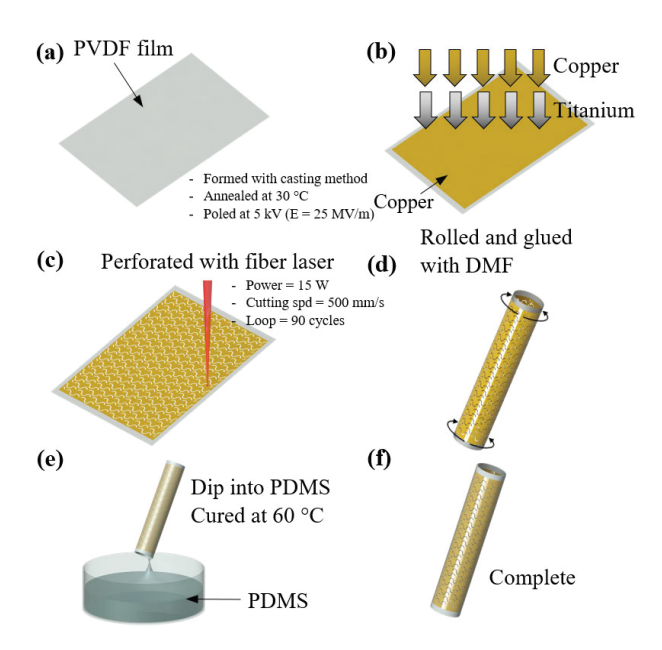


FIGURE 2. Fabrication process of Smart Stent. (a) Casting PVDF film, (b) metallization of both sides of the film with titanium and copper, (c) laser perforation, (d) rolling and gluing, (e) passivation with PDMS, and (f) Smart Stent completed.

III. RESULTS AND DISCUSSIONS

Fig. 3(a) presents the prototype of the smart stent, realized through the previously outlined processes. Initially, an assessment of the smart stent's pressure-sensing capability was conducted. For this purpose, a stent graft and an AAA model were fabricated using 3D printing techniques. The stent graft was fabricated using a natural rubber latex supported by a 3D printed stretchable frame that was modeled after a conventional stent design, as depicted in Fig. 3(b). The AAA's computer-aided design (CAD) model was sourced from the open-source website Thingiverse. Employing a laser-based 3D printer (Form 3, Formlabs Inc.) an elastic resin (Elastic 50A, Formlabs Inc.) was utilized to emulate the mechanical properties of the AAA. The customized stent graft was slightly crimped to allow the smart stent prototype to encase it, then, releasing the crimping ensured that the smart stent was securely mounted onto the stent graft, as showcased in Fig. 3(c). Subsequently, the smart stent was inserted into the 3D-printed AAA model, as illustrated in Fig. 3(d). Both terminations of the stent graft were firmly affixed to the inner wall of the AAA model using resin curing. The depiction in Fig. 3(d) conveys the partial configuration of the testing arrangement for the smart stent.

Fig. 4(a) provides an intricate overview of the experimental setup designed for evaluating the smart stent. The system is comprised of several key components meticulously assembled to mimic physiological conditions and facilitate testing as depicted in Fig. 4(a). An artificial blood reservoir serves as the fluid source, with two peristaltic pumps playing pivotal roles in the setup. Peristaltic pump 1, serving as the core of the system, continuously transports artificial blood from the reservoir into the 3D-printed AAA model

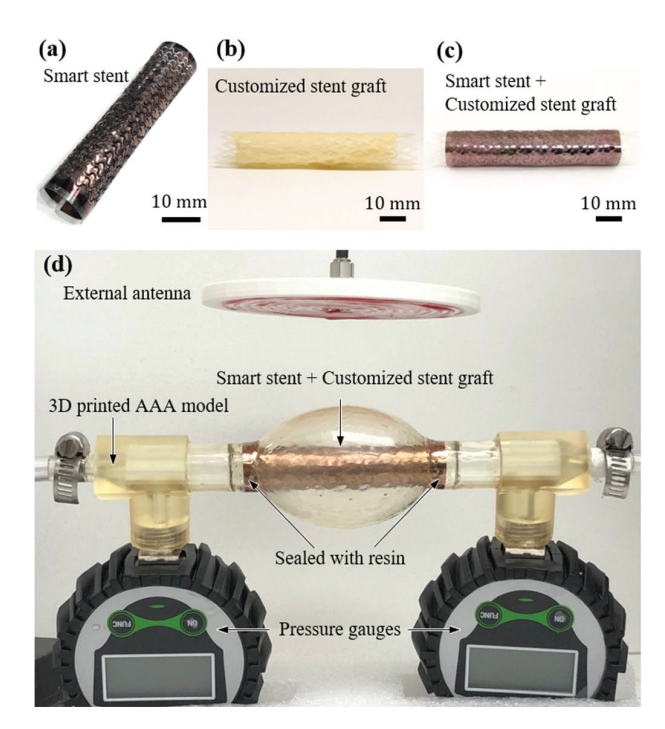
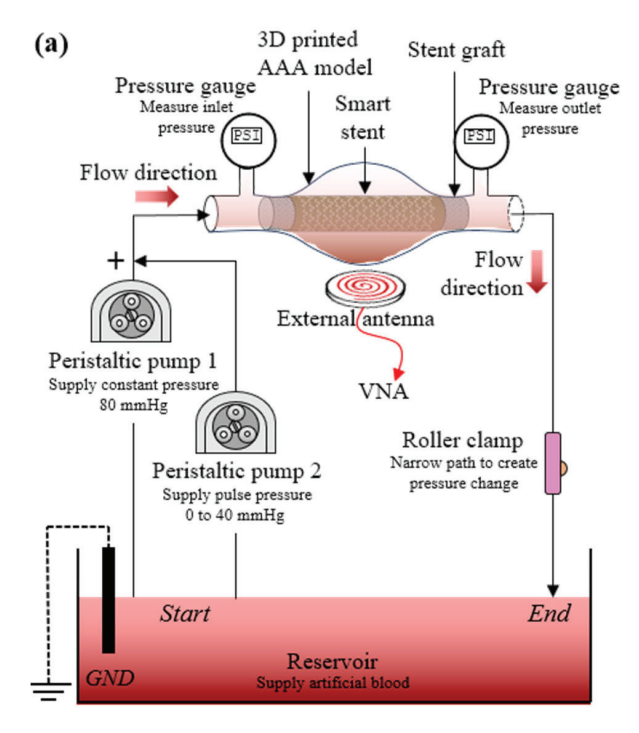


FIGURE 3. Fabrication results of the Smart Stent and the assembly of the 3D printed AAA model for testing. (a) Smart Stent, (b) Smart Stent inserted onto a 3D printed stent graft, and (c) Smart Stent and 3D printed stent graft inserted into a 3D printed AAA model with Y-coupler.

via PVC pipes. However, given the need to replicate the complex pressure waveform characteristic of human blood pressure (i.e., 80 mmHg for diastolic and 120 mmHg for systolic), peristaltic pump 2 was deployed to generate periodic pulses into the AAA model. A roller clamp was strategically positioned at the system's exit point, constricting the pipe and thereby introducing resistance along the exit path. This resistance effectively maintains elevated pressure levels within the AAA model. The AAA model itself, precisely constructed through 3D printing techniques, was seamlessly integrated with the smart stent to replicate realworld conditions accurately. The integration of pressure gauges at both the inlet and outlet of the AAA model facilitated the measurement of pressure variations within the system. These pressure gauges were connected to T-junctions, serving as crucial points for pressure monitoring, as shown in Fig. 4(b). An essential component of the setup was the planar inductor-based external antenna, strategically positioned at a distance from the AAA model to wirelessly monitor changes in internal pressure, represented as shifts in the natural resonance frequency of the smart stent through inductive coupling and analyzed using a Vector Network Analyzer (VNA) model 8753ES from Agilent Inc.

To validate the experimental apparatus as a representation of the human circulatory system, two experiments were conducted, and the results are depicted in Fig. 5. In the initial experiment, an average flow rate was established as the control variable, and the corresponding inlet pressures were measured accordingly. The average flow rate, denoted as 'v' and quantified in mL/min, was systematically varied





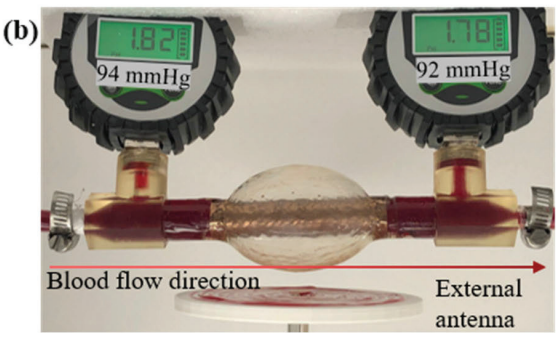


FIGURE 4. Testing system for the Smart Stent as a pressure sensor inside a 3D printed AAA model with two peristaltic pumps as the pressure generators. (a) Schematic of the testing setup, (b) photo of the testing setup highlighted the 3D printed AAA model with two pressure gauges (inlet and outlet), a valve, and a coupling inductor.

within the range of 940 to 1450 mL/min, utilizing 30 mL/min increments. This manipulation resulted in a spectrum of inlet pressures, represented as ' P_{in} ' and measured in mmHg, spanning from 60 to 140 mmHg, as shown in Fig. 5(a). The observed exponential rise in inlet pressure with increasing average flow rate underscores the inherent elastic properties of the 3D-printed stent graft within the experimental setup. The collected data were used to generate a fitting curve equation, achieving an impressive R-squared error of 0.9979, thus providing a robust mathematical representation of the relationship between average flow rate and inlet pressure. The fitting curve equation is

$$P_{in} = 11.84 \cdot e^{0.001728 \cdot \nu} \tag{1}$$

which allowed us to calculate the required flow rate for any given inlet pressure.

The second experiment aimed to confirm the consistency between inlet and outlet pressures across various pressure levels. In this experiment, the inlet pressure was designated as the control variable, ranging from 60 to 140 mmHg with 5 mmHg intervals, while corresponding outlet pressures were measured. The obtained R-squared value of 0.9997, as illustrated in Fig. 5(b), indicates a strong fit between the measured outlet pressures and the theoretically expected outlet pressures, which were assumed to match the inlet pressure. This outcome provides compelling evidence that the system losses were minimized, and unwanted leakage did not occur during pressurized conditions.

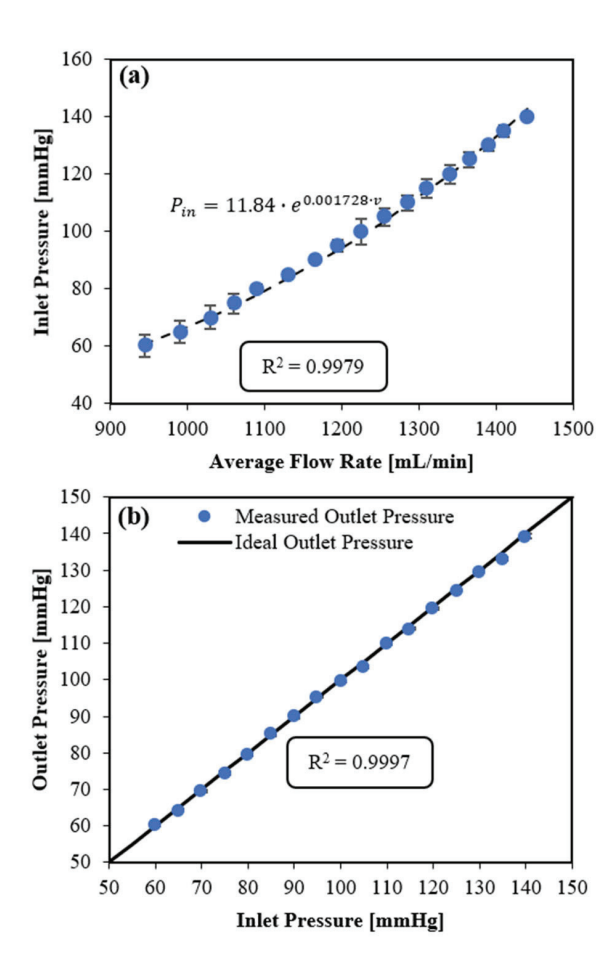


FIGURE 5. Characterization of the Smart Stent testing setup. (a) Average flow rate as control and inlet pressure as measurement, and (b) inlet pressure is controlled, and outlet pressure is measured.

Considering the smart stent is implanted within the human body, an external wireless sensing mechanism is required to extract data from the smart stent. As previously mentioned, the internal blood pressure change causes a geometrical deformation of the smart stent, inducing a natural resonance frequency shift. This periodic frequency shift can be wirelessly detected using an external antenna through inductive coupling. Inductive coupling is a common wireless transmission technique that has been widely implemented in implantable medical devices for various applications, such as power transfer [26], battery recharging [27], wireless data transmission [28], RFID [29], and telemetry [30]. In general, inductive coupling involves two coils interacting with each

VOLUME 12, 2024 198127

other through magnetic field [31]. In the case of the smart stent, the external antenna serves as the primary coil, and the resonant frequency shift of the smart stent, which acts as the secondary coil, is wirelessly detected by the external antenna. The detected frequency shift is further decoded into pressure measurements, enabling wireless data transmission through inductive coupling. The external antenna, a singlearm spiral antenna, was designed as the core component for wireless monitoring of the resonance frequency shift of the smart stent across various pressure levels in the system, as shown in Fig. 6(a) [26]. The single-arm spiral antenna consists of 22-gauge metal wires and a polylactic acid (PLA) substrate. It has a spacing of 2 mm between each turn of the coil and the number of turns was 10, resulting in an overall diameter of the antenna of 10 cm, with a height of 5.5 mm. The designed antenna was simulated from 100 to 120 MHz using a commercial 3D EM simulator, a finite element highfrequency structure simulation (HFSS) software from Ansys Electronics Desktop. The external antenna was also simulated with the smart stent positioned 10 cm above it, as shown in Fig. 6(b). Fig. 6(c) shows the simulated and measured return loss (S11) of the external antenna with and without the smart stent. The simulated external antenna showed a resonant frequency at 111.50 MHz with a return loss of -12.50 dB without the smart stent. When a smart stent was positioned 10 cm above it, the resonance frequency of the external antenna shifted to 110.05 MHz with a return loss of -14.69 dB. In measurement, the external antenna showed a resonant frequency of 111.18 MHz with a return loss of -12.27 dB without the smart stent and a resonant frequency of 109.69 MHz with -14.17 dB with the smart stent. The measured results of the external antenna, both with and without the smart stent, matched well with the simulated results. The differences between the simulated and measured resonance frequency in both cases were only 0.32 MHz and 0.36 MHz. This comparison demonstrates that the external antenna is reliably characterized and can monitor the resonance frequency shift accurately.

To optimize the external antenna performance, the external antenna was subjected to testing with a piece of tissue located in between the external antenna and the smart stent, as illustrated in Fig. 7(a). In this case, a 3-cm thick pork belly was used as the tissue for the experiment to emulate the complex composition of the human body around the AAA [32], [33]. Due to the irregular shape of the tissue, the closest feasible measuring distance was approximately 0.5 cm. During the investigation, one would expect the smaller gap size between the tissue and the external antenna to yield higher sensitivity and accuracy, whereas a larger gap size yields lower sensitivity and accuracy. However, contrary to expectations, we observed otherwise. The experiment was conducted by varying the gap size between the external antenna and the tissue from 0.5 to 5 cm in 0.5 cm increments. A constant internal pressure of 100 mmHg was maintained throughout the experiment, which served as our reference data, and the resonance frequencies were measured; the

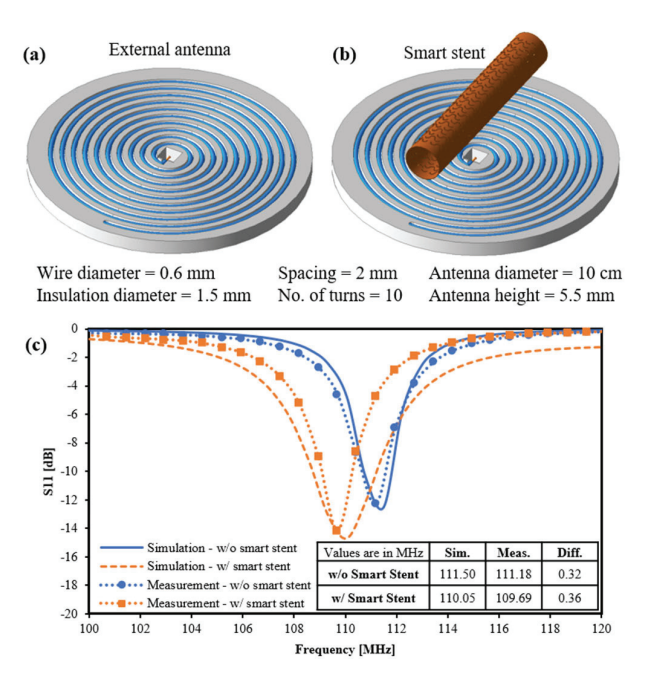


FIGURE 6. Design and characterization results of the single-arm spiral antenna with and without the presence of the smart stent. (a) Illustration of the external antenna. (b) Illustration of the external antenna with the smart stent placed 10 cm above it. (c) Comparison between the simulation and the measurement results with and without smart stent.

results are presented in Fig. 7(b). We observed that the resonance frequency started with two peaks at a gap size of 0.5 cm, reaching the highest S11 of -31.06 dB at a frequency of 106.10 MHz with a gap size of 1.5 cm, before slowly decreasing as the gap size increased. Therefore, the optimal placement of the external antenna was 1.5 cm away from the tissue surface, offering the highest sensitivity and accuracy for measuring the frequency shift. Furthermore, we conducted similar experiments but using different tissue thicknesses ranging from 4 cm to 7 cm to find the optimal gap size, and the results are shown in Fig. 7(c). Similarly, the external antenna yielded the highest S11 when placed 1.5 cm away from the tissue surface. The results suggested that doctors or patients can conveniently perform post-EVAR surveillance wirelessly by positioning the external antenna 1.5 cm from the patient regardless of the size of the patient. Lastly, the resonance frequencies of the external antenna with and without the presence of tissue at various measuring distances were compared to investigate the amount of frequency shifting caused by the tissue. Note that the measuring distance was the distance between the smart stent and the external antenna as indicated in Fig. 7(a). Fig. 7(d) demonstrates that the average resonance frequency without tissue was measured to be 109.77 ± 0.44 MHz, whereas the average resonance frequency shifted to 106.37 \pm 0.29 MHz when a tissue was present. The frequency shift by the tissue was computed to be 3.4 MHz, approximately 3.09 % of the original resonance frequency, which is acceptable in this application.



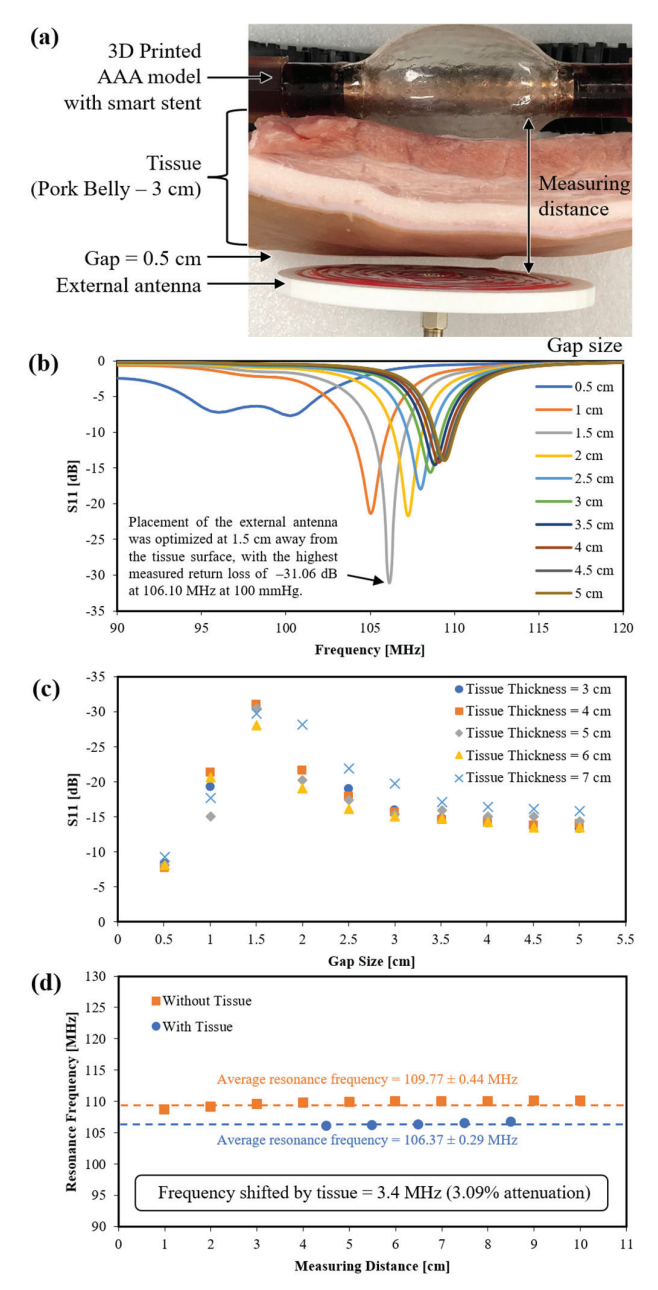


FIGURE 7. Optimization of the wireless sensing performance by the external antenna with various tissue thicknesses and measuring distances at 100 mmHg. (a) Experimental setup with tissue positioned in between the external antenna and the smart stent when 100 mmHg blood pressure was applied. (b) Measured resonance frequency at various gap sizes (0.5 to 5 cm) at 100 mmHg. (c) Comparison results of different tissue thicknesses (3 to 7 cm). (d) Frequency shifting when a tissue was placed between the smart stent and the antenna.

In an ideal case, the stent graft should conform to the biomechanics of a vascular structure, expanding under systolic pressure. This expansion induces deformation in the encapsulated smart stent, leading to a subtle shift in its natural resonance frequency. As previously mentioned, this subtle natural resonance frequency shift can be wirelessly detected using an external antenna, specifically through inductive coupling. Fig. 8(a) demonstrates the measured S11 when the tissue thickness was 4 cm, and the external

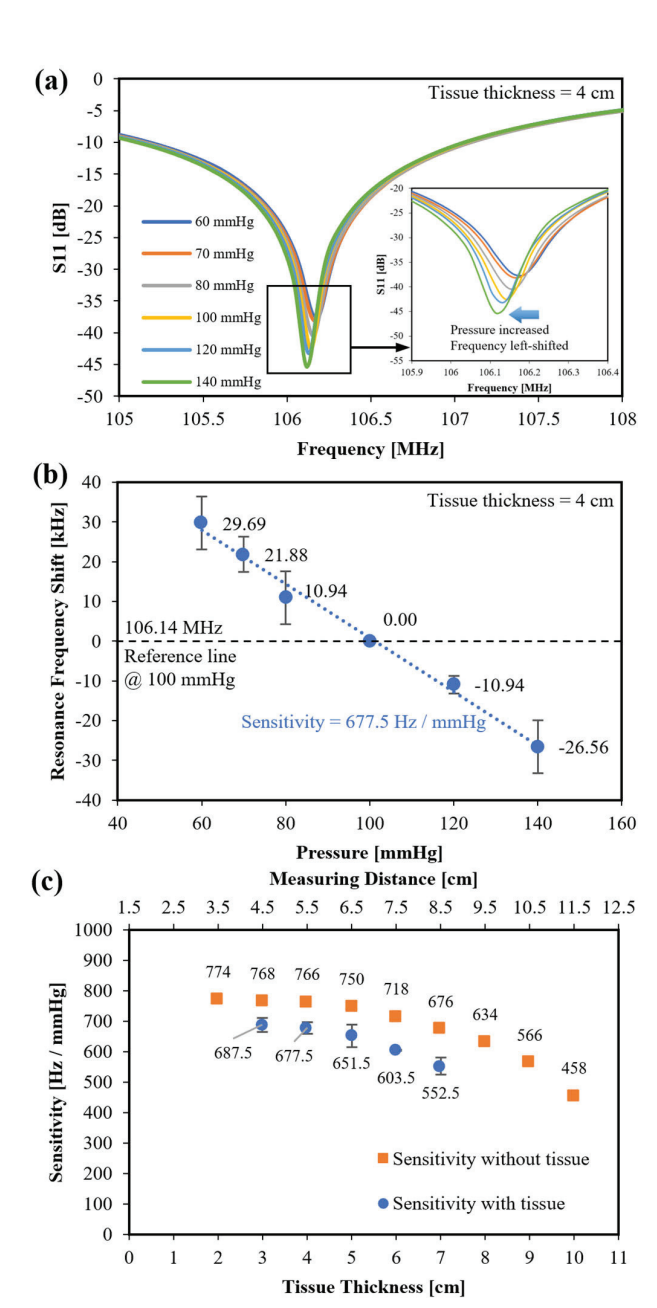


FIGURE 8. Resonance frequency shifts measurement results at various pressures (60 to 140 mmHg) and different tissue thicknesses (3 to 7 cm). (a) Resonance frequency shifted from high to low when pressure increased. (b) Magnitude of frequency shifting when centered around 100 mmHg. (c) Smart stent sensitivity towards pressure changes with and without tissue at various tissue thicknesses (3 to 7 cm) or measuring distances (3.5 to 11.5 cm).

antenna was placed 1.5 cm from the tissue with the pressures varying from 60 to 140 mmHg. A clear high-to-low frequency shifting pattern was observed when the pressure increased. In Fig. 8(b), considering the resonance frequency of 106.14 MHz at the pressure 100 mmHg as the reference point, the resonance frequency rises or drops by roughly 30 kHz as the pressure decreases or increases, respectively. A consistent trend emerged from the data, presenting a sensitivity of 677.5 Hz/mmHg when the tissue thickness was 4 cm. Similar experiments were conducted to

VOLUME 12, 2024 198129



examine the sensitivity for various tissue thicknesses (3 to 7 cm). In Fig. 8(c), we observed a descending pattern for the sensitivity as the tissue thickness increased. For comparison, the sensitivity of the external antenna without the tissue was measured. We discovered the sensitivity was reduced by 9 to 20% depending on the tissue thickness. Despite the observed tissue thickness dependency, all measuring distances exhibited similar frequency shifts, transitioning linearly from higher to lower frequencies as internal pressure increased. These findings collectively affirm the smart stent's capability as a wireless pressure sensor.

IV. CONCLUSION

In conclusion, this study presented the development and assessment of a smart stent featuring wireless pressuresensing capabilities, offering a potential solution to several challenges associated with post-EVAR surveillance. These challenges encompassed issues such as high costs, protracted scanning procedures, substantial radiation exposure, and patient discontinuation. The fabrication of the smart stent involved the use of a piezoelectric material, which was meticulously laser-perforated with an array of patterns to optimize voltage generation and pressure sensitivity. This fabricated smart stent was seamlessly integrated into a 3Dprinted stent graft, which was securely implanted within a 3D-printed elastic AAA model. The functionality of the smart stent as a wireless pressure sensor was validated by measuring its resonance frequency through inductive coupling via an external antenna. Experimental results demonstrated a consistent linear shift in the resonance frequency with increasing pressure within the stent graft. Notably, the sensitivity of the smart stent to pressure changes increased as the tissue thickness decreased, with a maximum sensitivity of 687.5 Hz/mmHg achieved at a tissue thickness of 3 cm. Despite this, there is considerable room for improvement in terms of sensitivity, either by introducing a dedicated capacitive pressure sensing mechanism instead of solely relying on the natural resonant frequency shifting or by incorporating an active transmitter module powered by the harvested energy from the proposed smart stent. Nevertheless, this innovative smart stent exhibits key characteristics that position it as a cost-effective alternative for routine EVAR monitoring. Its potential benefits encompass reduced hospital visit frequency, shorter hospital visit durations, minimized complications, and enhancements in the quality of life for patients undergoing EVAR procedures.

REFERENCES

- [1] B. Keisler and C. Carter, "Abdominal aortic aneurysm," *Amer. Family Physician*, vol. 91, no. 8, pp. 538–543, Apr. 2015.
- [2] A. Schanzer and G. S. Oderich, "Management of abdominal aortic aneurysms," New England J. Med., vol. 385, no. 18, pp. 1690–1698, Oct. 2021, doi: 10.1056/nejmcp2108504.
- [3] A. Thapar, D. Cheal, T. Hopkins, S. Ward, J. Shaloub, and S. Yusuf, "Internal or external wall diameter for abdominal aortic aneurysm screening?" Ann. Roy. College Surgeons England, vol. 92, no. 6, pp. 503–505, Sep. 2010, doi: 10.1308/003588410x12699663903430.

- [4] N. Sakalihasan, R. Limet, and O. Defawe, "Abdominal aortic aneurysm," *Lancet*, vol. 365, no. 9470, pp. 1577–1589, Apr. 2005, doi: 10.1016/s0140-6736(05)66459-8.
- [5] A. England and R. McWilliams, "Endovascular aortic aneurysm repair (EVAR)," *Ulster Med. J.*, vol. 82, no. 1, pp. 3–10, Jan. 2013.
- [6] H. O. Kim, N. Y. Yim, J. K. Kim, Y. J. Kang, and B.-C. Lee, "Endovascular aneurysm repair for abdominal aortic aneurysm: A comprehensive review," *Korean J. Radiol.*, vol. 20, no. 8, pp. 1247–1265, Jan. 2019.
- [7] J. A. van der Vliet, L. J. Schultze Kool, and F. van Hoek, "Simplifying post-EVAR surveillance," Eur. J. Vascular Endovascular Surg., vol. 42, no. 2, pp. 193–194, Aug. 2011, doi: 10.1016/j.ejvs.2011.04.012.
- [8] T. Smith and K. B. Quencer, "Best practice guidelines: Imaging surveillance after endovascular aneurysm repair," *Amer. J. Roentgenol.*, vol. 214, no. 5, pp. 1165–1174, May 2020, doi: 10.2214/ajr.19.22197.
- [9] D. Daye and T. G. Walker, "Complications of endovascular aneurysm repair of the thoracic and abdominal aorta: Evaluation and management," *Cardiovascular Diagnosis Therapy*, vol. 8, no. S1, pp. S138–S156, Apr. 2018.
- [10] A. Schanzer, L. M. Messina, K. Ghosh, J. P. Simons, W. P. Robinson, F. A. Aiello, R. J. Goldberg, and A. B. Rosen, "Follow-up compliance after endovascular abdominal aortic aneurysm repair in medicare beneficiaries," *J. Vascular Surg.*, vol. 61, no. 1, pp. 16–22, Jan. 2015, doi: 10.1016/j.jvs.2014.06.006.
- [11] M. J. Grima et al., "Multicentre post-EVAR surveillance evaluation study (EVAR-SCREEN)," Eur. J. Vascular Endovascular Surg., vol. 57, no. 4, pp. 521–526, Apr. 2019, doi: 10.1016/j.ejvs.2018.10.032.
- [12] J. Vishnu and G. Manivasagam, "Perspectives on smart stents with sensors: From conventional permanent to novel bioabsorbable smart stent technologies," *Med. Devices Sensors*, vol. 3, no. 6, Dec. 2020, Art. no. e10116, doi: 10.1002/mds3.10116.
- [13] X. Chen, B. Assadsangabi, D. Brox, Y. Hsiang, and K. Takahata, "A pressure-sensing smart stent compatible with angioplasty procedure and its in vivo testing," in *Proc. IEEE 30th Int. Conf. Micro Electro Mech. Syst. (MEMS)*, Jan. 2017, pp. 133–136, doi: 10.1109/MEM-SYS.2017.7863358.
- [14] N.-E. Oyunbaatar, A. Shanmugasundaram, K. Kwon, and D.-W. Lee, "Continuous monitoring of cardiovascular function with a smart stent incorporating a flexible and stretchable wireless pressure sensor," *J. Micromech. Microeng.*, vol. 33, no. 11, Sep. 2023, Art. no. 115001, doi: 10.1088/1361-6439/acf7ce.
- [15] I. C. T. Santos, J. M. R. S. Tavares, L. A. Rocha, S. M. Sampaio, and R. Roncon-Albuquerque, "A possibility for pos-EVAR surveillance: A novel smart stent-graft," in *Technology and Medical Sciences*, 1st ed., Boca Raton, FL, USA: CRC Press, 2011, p. 4.
- [16] J. Park, J.-K. Kim, S. A. Park, and D.-W. Lee, "Biodegradable polymer material based smart stent: Wireless pressure sensor and 3D printed stent," *Microelectron. Eng.*, vol. 206, pp. 1–5, Feb. 2019, doi: 10.1016/j.mee.2018.12.007.
- [17] C.-H. Liu, S.-C. Chen, and H.-M. Hsiao, "A single-connector stent antenna for intravascular monitoring applications," *Sensors*, vol. 19, no. 21, p. 4616, Oct. 2019, doi: 10.3390/s19214616.
- [18] C. Occhiuzzi, G. Contri, and G. Marrocco, "Design of implanted RFID tags for passive sensing of human body: The STENTag," *IEEE Trans. Antennas Propag.*, vol. 60, no. 7, pp. 3146–3154, Jul. 2012, doi: 10.1109/TAP.2012.2198189.
- [19] J. Y. Tan, S. Islam, Y. Li, A. Kim, and J. Kim, "An optimization of perforation design on a piezoelectric-based smart stent for blood pressure monitoring and low-frequency vibrational energy harvesting," in *Proc. IEEE 36th Int. Conf. Micro Electro Mech. Syst. (MEMS)*, Jan. 2023, pp. 396–399, doi: 10.1109/MEMS49605.2023.10052623.
- [20] S. Islam, X. Song, E. T. Choi, J. Kim, H. Liu, and A. Kim, "In vitro study on smart stent for autonomous post-endovascular aneurysm repair surveillance," *IEEE Access*, vol. 8, pp. 96340–96346, 2020.
- [21] X. Zhang, L. Zhang, M. Li, W. Chen, J. Chen, Y.-J. Liu, and Y. Wang, "Research advances in hierarchically structured PVDF-based all-organic composites for high-energy density capacitors," *Membranes*, vol. 12, no. 3, p. 274, Feb. 2022, doi: 10.3390/membranes12030274.
- [22] A. E. Kennelly, F. A. Laws, and P. H. Pierce, "Experimental researches on skin effect in conductors," *Trans. Am. Inst. Electr. Eng.*, vol. 34, no. 2, pp. 1953–2021, Jul. 1915, doi: 10.1109/T-AIEE.1915.4765283.
- [23] R. Lay, G. S. Deijs, and J. Malmström, "The intrinsic piezoelectric properties of materials—A review with a focus on biological materials," *RSC Adv.*, vol. 11, no. 49, pp. 30657–30673, Sep. 2021, doi: 10.1039/d1ra03557f.



- [24] P. Hangge, Y. Pershad, A. A. Witting, H. Albadawi, and R. Oklu, "Three-dimensional (3D) printing and its applications for aortic diseases," *Cardiovascular Diagnosis Therapy*, vol. 8, no. S1, pp. S19–S25, Apr. 2018, doi: 10.21037/cdt.2017.10.02.
- [25] V. F. Cardoso, G. Minas, C. M. Costa, C. J. Tavares, and S. Lanceros-Mendez, "Micro and nanofilms of poly(vinylidene fluoride) with controlled thickness, morphology and electroactive crystalline phase for sensor and actuator applications," *Smart Mater. Struct.*, vol. 20, no. 8, Jul. 2011, Art. no. 087002.
- [26] A. Aldaoud, J.-M. Redoute, K. Ganesan, G. S. Rind, S. E. John, S. M. Ronayne, N. L. Opie, D. J. Garrett, and S. Prawer, "Near-field wireless power transfer to stent-based biomedical implants," *IEEE J. Electromagn.*, *RF Microw. Med. Biol.*, vol. 2, no. 3, pp. 193–200, Sep. 2018, doi: 10.1109/JERM.2018.2833386.
- [27] A. Bussooa, S. Neale, and J. R. Mercer, "Future of smart cardio-vascular implants," *Sensors*, vol. 18, no. 7, p. 2008, Jun. 2018, doi: 10.3390/s18072008.
- [28] B. John, C. Spink, M. Braunschweig, R. Ranjan, D. Schroeder, A. Koops, G. Woldt, I. Rauh, A. Leuzinger, G. Adam, and W. H. Krautschneider, "A stent graft occlusion detection: Pressure sensing implant device with inductive power and data telemetry," in *Proc. IEEE Int. Symp. Circuits Syst. (ISCAS)*, May 2018, pp. 1–4, doi: 10.1109/ISCAS.2018.8351667.
- [29] D. S. Brox, "A study of methodology and technology for wireless monitoring of blood pressure inside a stent," Dept. Elect. Comput. Eng., Univ. Brit. Columbia, Vancouver, BC, Canada, 2014, doi: 10.14288/1.0167345.
- [30] X. Chen, D. Brox, B. Assadsangabi, Y. Hsiang, and K. Takahata, "Intelligent telemetric stent for wireless monitoring of intravascular pressure and its in vivo testing," *Biomed. Microdevices*, vol. 16, no. 5, pp. 745–759, Oct. 2014, doi: 10.1007/s10544-014-9879-8.
- [31] K. S. Nikita, Handbook of Biomedical Telemetry. Hoboken, NJ, USA: Wiley, 2014.
- [32] G. Pafitanis, D. Veljanoski, A. M. Ghanem, and S. Myers, "Pork belly: A simulation training model for intramuscular perforator dissection," *Plastic Reconstructive Surg.*, *Global Open*, vol. 6, no. 2, Feb. 2018, Art. no. e1674, doi: 10.1097/gox.0000000000001674.
- [33] X. Wang, Y. Albahrani, M. Pan, and J. Levitt, "Skin simulators for dermatological procedures," *Dermatol. Online J.*, vol. 21, no. 11, pp. 1–10, Nov. 2015.



JUN YING TAN (Member, IEEE) received the B.S. degree in electrical and computer engineering from Kansas State University, Manhattan, KS, USA, in 2018. He is currently pursuing the Ph.D. degree in electrical engineering with the University of North Texas, Denton, TX, USA.

His research interests include the design and fabrication of various kinds of microneedles, implementation of multi-modal electrochemicalbased sensors, development and optimization of

implantable pressure sensing devices, and wireless communication applications.



CHEOLBOK KIM received the Ph.D. degree in electrical engineering from the University of Florida, Gainesville, FL, USA, in 2014. He was a Senior Research Engineer with LG Innotek, Ansan, South Korea, from 2014 to 2017, and with LG Electronics, Seoul, South Korea, from 2017 to 2018. He has been a Senior Research Scientist with the Department of Research and Development, Corning Inc., Corning, NY, USA, since 2018. He has authored one book chapter,

more than 50 peer-reviewed articles, and holds seven patents, including two U.S. patents. His current research interests include millimeter-wave (mmwave) and terahertz (THz) antenna/RF/antenna-in-packaging for 5G/6G

wireless communications, material characterization and measurement techniques at mm-wave and THz, automotive radar, frequency selective surface, metamaterial, microfabrication, and optimization algorithm. He was a recipient of the IEEE Antenna and Propagation Society Doctoral Research Award, in 2013.



TRISHA DAS MOU received the bachelor's degree in electrical and electronics engineering from the International University of Business Agriculture and Technology (IUBAT), Bangladesh, with prestigious academic scholarships. She is currently pursuing the Ph.D. degree with the Medical Engineering Department, in Summer 2023. Her research interests include nanotechnology, piezoelectric microsystems, wireless implantable biomedical sensors, embedded microelectronics,

and implantable biomedical devices.



ALBERT KIM received the B.S., M.S., and Ph.D. degrees from Purdue University, in 2008, 2010, and 2015, respectively. He was an Assistant Professor with the Department of Electrical and Computer Engineering, Temple University, from 2017 to 2022. He was also a Research and Development Engineer with Intel Corporation before joining a faculty position. He is currently an Assistant Professor with the Department of Medical Engineering, University of South Florida

(USF). His research has been founded on Acousto-Bioelectronics, a branch of electrical engineering that studies the use of sound waves in the Biomedical Microelectromechanical System (BioMEMS) and nanotechnology. This includes a variety of devices and microsystems to address important clinical problems, including cancer, cardiovascular monitoring, and dental. Their group collaborates closely with physicians in order to transfer the technology to the clinic. His research on a novel electromechanical interrogation scheme and a wearable gait analyzer has been featured in news media, such as Fox News, Science Magazine, Chicago Tribute, Engadget, and Popular Science. He has co-authored more than 50 publications in prestigious journals, international conferences, and patents.



JUNGKWUN 'JK' KIM (Member, IEEE) received the master's and Ph.D. degrees from the State University of New York at Buffalo, in 2007 and 2011, respectively. He was a Research Faculty with the University of Pennsylvania, from 2013 to 2016, and has two years of experience as a Postdoctoral Fellow with Georgia Institute of Technology, from 2011 to 2013. In 2016, he became an Assistant Professor with the Department of Electrical and Computer Engineering, Kansas State Univer-

sity. In 2022, he joined the Department of Electrical Engineering, University of North Texas as an Associate Professor. Throughout his career, he has been dedicated to leveraging nanotechnology and microfabrication to tackle various engineering challenges. His research efforts primarily revolve around the development of 3D microfabrication techniques and their applications in fields, such as biomedical engineering, RF/microwave/THz technology, and optical devices. This innovative work takes place within his Advanced Nano Micro Electronics Laboratory.

VOLUME 12, 2024 198131

. . .